JGR Space Physics

RESEARCH ARTICLE
10.1029/2021JA029514

Key Points:

- Simultaneous observation of an Electromagnetic Ion Cyclotron (EMIC) wave event by THEMIS A, D, and E separated by a few 1,000 km
- Source regions of EMIC waves are scattered around the equator close to the magnetopause
- The subpackets drastically change their amplitudes and frequencies within one wavelength of EMIC waves

Correspondence to:
B. Ojha,
bojha92@gmail.com

Citation:
Ojha, B., Omura, Y., Singh, S., & Lakhina, G. S. (2021). Multipoint analysis of source regions of EMIC waves and rapid growth of subpackets. *Journal of Geophysical Research: Space Physics*, *126*, e2021JA029514. https://doi.org/10.1029/2021JA029514

Received 30 APR 2021
Accepted 13 OCT 2021

Author Contributions:
Conceptualization: Biswajit Ojha, Yoshiharu Omura, Satyavir Singh
Formal analysis: Biswajit Ojha
Funding acquisition: Yoshiharu Omura, Satyavir Singh
Investigation: Biswajit Ojha, Yoshiharu Omura
Methodology: Biswajit Ojha, Yoshiharu Omura, Satyavir Singh
Project Administration: Yoshiharu Omura, Satyavir Singh
Resources: Biswajit Ojha
Software: Biswajit Ojha
Supervision: Yoshiharu Omura, Satyavir Singh, Gurbax S. Lakhina
Validation: Biswajit Ojha, Yoshiharu Omura, Satyavir Singh, Gurbax S. Lakhina
Visualization: Biswajit Ojha, Yoshiharu Omura, Gurbax S. Lakhina
Writing – original draft: Biswajit Ojha
Writing – review & editing: Biswajit Ojha, Yoshiharu Omura, Satyavir Singh, Gurbax S. Lakhina

Multipoint Analysis of Source Regions of EMIC Waves and Rapid Growth of Subpackets

Biswajit Ojha[1], Yoshiharu Omura[2], Satyavir Singh[1], and Gurbax S. Lakhina[1]

[1]Indian Institute of Geomagnetism, Navi Mumbai, India, [2]Research Institute for Sustainable Humanosphere (RISH), Kyoto University, Kyoto, Japan

Abstract Electromagnetic Ion Cyclotron (EMIC) rising tone emissions are important in understanding the nonlinear wave evolution and interaction with the energetic particles. We present observations of rising tone emissions of EMIC waves by THEMIS A, D, and E spacecraft in the outer magnetosphere. These emissions with subpacket structures in the proton band were observed during the time interval 14:20 UT to 14:30 UT on September 9, 2010. The observed waves are left-handed polarized with wave normal angles less than 30°. THEMIS A was closest to the equator and was in a higher L-shell than THEMIS E and D. The smallest radial separation is ~2,000 km between THEMIS E and D spacecraft. This configuration of THEMIS allows us to investigate the subpackets of rising tone EMIC waves observed simultaneously at 14:23 UT by three spacecraft. Hilbert Huang Transformation (HHT) is applied to show the variations of the instantaneous frequency and the observed wave amplitude. The direction of energy flow is determined from the analysis of the Poynting flux. There is a rapid nonlinear growth of the EMIC subpackets within one wavelength. Subpackets are dynamic in nature as their structure changes within one wave period, which is further supported by the nonlinear wave growth theory. Optimum and threshold amplitudes for the EMIC wave growth are calculated beside the nonlinear transition time (T_N). Observed ion energies and pitch angle spectra of the ion fluxes are consistent with the energy associated with the Landau and cyclotron resonance conditions.

Plain Language Summary Electromagnetic Ion Cyclotron (EMIC) waves are observed below the proton gyrofrequency and play an important role in the magnetospheric dynamics through the ion heating and precipitation of relativistic electrons. They often appear as a series of repetitive structures (known as subpackets) with increasing frequencies, known as rising tone emissions in their entirety. These rising tone emissions are believed to be generated near the geomagnetic equator by the anisotropic distribution of energetic ions ($\frac{T_\perp}{T_\parallel} > 1$). These emissions are self-sustaining after the primary linear growth of the triggering wave at lower frequencies. Although previous simulations and theory showed that the source regions of these rising tone emissions move along the magnetic field line, direct observational evidence was missing. Our article provides a case study where these emissions are observed simultaneously by three THEMIS probes in the outer magnetosphere. Adopting a multipoint observation technique, we show there are scattered source regions with an extent greater than the EMIC wavelength, and the subpacket structure changes nonlinearly within one wave period. This analysis provides crucial information about the dynamics of the fine structures of rising emissions and gives an idea about the 3D extent of subpackets.

1. Introduction

Electromagnetic ion cyclotron (EMIC) waves are important from the point of view of understanding the wave-particle interactions in the Earth's magnetosphere and their role in acceleration and heating of particles, precipitation of ring current ions and relativistic electrons, and dropout phenomena (Clilverd et al., 2015; Cornwall & Schulz, 1971; Kersten et al., 2014; Summers & Thorne, 2003; Summers et al., 1998, 2007; Thorne & Horne, 1992, 1997; Thorne & Kennel, 1971; Zhu et al., 2020). These low frequency, left handed polarized waves falls in the range of Pc1-Pc2 (Jacobs et al., 1965). They are amplified near the geomagnetic equator (~ ±11°magnetic latitude (MLAT)) by the hot proton (H^+) temperature anisotropy ($\frac{T_\perp}{T_\parallel} > 1$) (Allen et al., 2015; Cornwall, 1965; Cornwall & Schulz, 1971; Kivelson & Russell, 1995; Loto'Aniu et al., 2005). These waves propagate along the magnetic field line and the wave normal angle (WNA) become oblique during their

propagation to higher latitudes. In a multi-species plasma, the dispersion shows there are stop bands for L-modes (e.g., H^+, He^+, O^+, etc.). Although mostly these waves are identified by observing the spectra of the electromagnetic field fluctuations, the L-mode dispersion relation can be seen from the observational data. Pakhotin et al. (2013) and Vines et al. (2021) have estimated the k-vector directly from observations. These L-mode waves change their polarization from left to right near the crossover frequency to propagate further through the stop bands. The crossover frequency is where the phase speeds of L- and R-modes coincide, and wave shows linear polarization. These quasi-parallel waves propagating toward higher latitudes reflect at the bi-ion frequency (Horne & Thorne, 1993) where the WNA becomes 90°. In the source region, the EMIC waves propagate both parallel and anti-parallel to the magnetic field line showing bidirectionality within ~±11° MLAT (Allen et al., 2013; Liu et al., 2013; Loto'Aniu et al., 2005). This idea is further tested in several theoretical and numerical studies. Around the bifurcated magnetic minima, the anisotropy of the energetic particles becomes maximum, which is the source of the generation of off-equator EMIC waves in the outer magnetosphere. Combined roles of Shabansky orbits and drift shell splitting for EMIC wave growth at higher shells are studied in detail by McCollough et al. (2009, 2012) and McCollough et al. (2010). The addition of realistic particle fluxes (e.g., AP-8; see McCollough et al., 2009) can turn off the anisotropy generated by drift shell splitting. There can exist the anisotropy for the energetic particles following Shabansky orbits. For the first time, Tsurutani and Smith (1977) have introduced very low-frequency wave generation because of Shabansky orbits and drift shell splitting. Though Allen et al. (2013) and Liu et al. (2013) have reported bidirectional EMIC wave propagation in the off-equator region, the source of their generation was not identified for sure. Recently, Vines et al. (2019) showed with the Magnetospheric Multiscale (MMS) data that the local source regions for higher latitudes EMIC wave growth occur for several hours in the outer magnetosphere, and they have ruled out the possibility of the reflection at a critical bi-ion frequency and established the local generation sources for off-equator EMIC wave growth.

There have been several observations looking into the size of EMIC source regions (e.g., Blum et al., 2017; Engebretson et al., 2008, 2015; Lee & Angelopoulos, 2014; Mann et al., 2014; Zhang et al., 2016). However, only very recently Hendry et al. (2020) determined the latitudinal extension of the source regions with the combination of multi-spacecraft and ground-based measurements. They reported ~0.67° latitudinal drift with a drift rate of the source region ~4°/h and longitudinal drift ~11°/h. Moreover, they investigated the magnetic local time (MLT) extent of the source region ~0.83 h, which is almost stationary. Although they observed EMIC wave signatures for several hours, they did not take into account the subpacket structures (Omura & Zhao, 2012; Omura et al., 2010; Shoji & Omura, 2012, 2013, 2017). Sakaguchi et al. (2015) discussed the isolated proton aurora (IPA) and reported its longitudinal extension to be ~12°. Investigation by Lee et al. (2013) showed H^+-band EMIC waves can span $\geq 1 R_E$ at $L > 6$. However, the source region extension near dayside magnetopause is still not understood completely. Previous studies (Blum et al., 2017; Grison et al., 2013) have shown the spatial and temporal extents of regions of EMIC wave activity, their local time, and radial distance dependence in the magnetosphere. However, wavelength and the size of the source region of the triggered EMIC emissions have not been explored. Further, it is an unanswered question of what dimension along and across the field line is needed to form a series of rising tone subpackets that can be observed at a particular position.

EMIC waves can accelerate the energetic ions through cyclotron resonance interaction. When wave resonance velocity is comparable to the thermal speed of the plasma species, the wave can either gain energy leading to wave growth or provide energy to the species resulting in the damping of the wave. This mechanism is generally called the cyclotron resonance interaction, which deals with kinetic plasma theory where the particle distribution function decides the growth or damping of the waves (Tsurutani & Lakhina, 1997). These waves can contribute to intense pitch angle scattering of the particles in the outer radiation belt, pushing them into the loss cone, and therefore resulting in loss of particles into the lower atmosphere (Tsurutani & Smith, 1977).

Many spacecraft observations (e.g., Cluster, THEMIS, Van Allen Probes, MMS, etc.) have found the fine structure rising tone of EMIC waves (Grison et al., 2013; Nakamura et al., 2015; Pickett et al., 2010; Shoji & Omura, 2012, 2017). The generation of the EMIC triggered emission is caused by a resonant interaction of the protons with the triggered waves around the proton hole (Omura et al., 2010). The self-sustaining frequency rising process of these waves is also discussed in Shoji and Omura (2013). In four events from

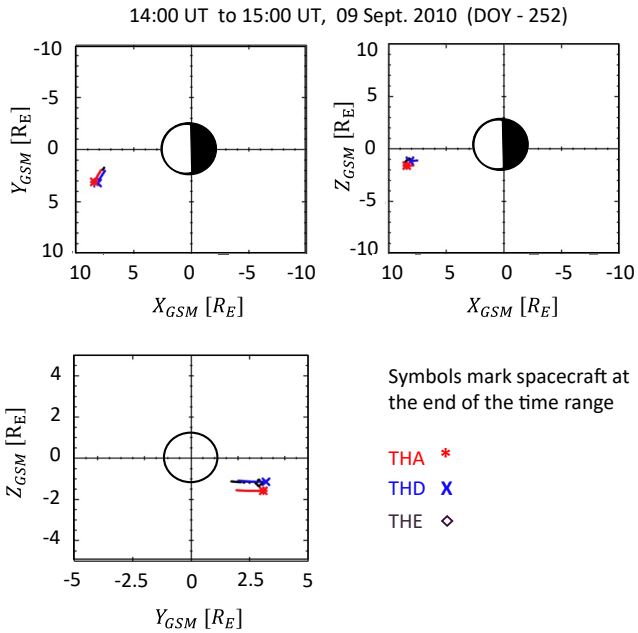

Figure 1. Position of the spacecraft in GSM coordinate are shown for September 9, 2010 (DOY 252) from 14:00 UT to 15:00 UT. spacecraft symbols: THA→ red asterisk, THD→ blue X, THE→ black diamond. All are well inside the magnetopause ~8 R_e from the Earth.

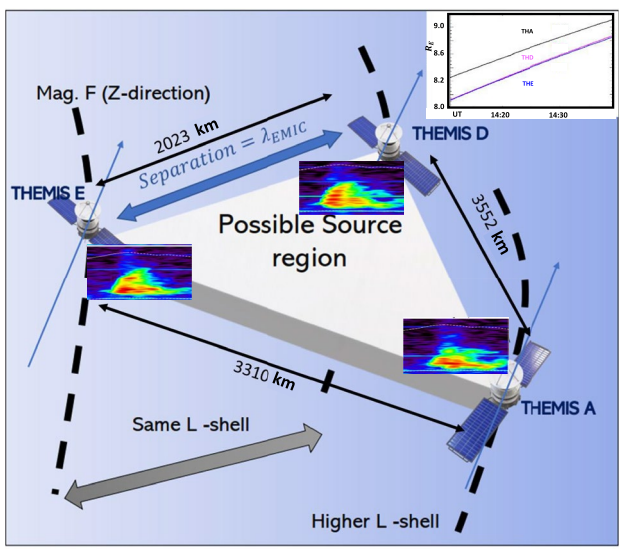

Figure 2. Cartoon of the THEMIS constellation during the observed Electromagnetic Ion Cyclotron (EMIC) waves on September 9, 2010. Inset: Distance from the Earth in R_E for THA (black), THD (magenta) and THE (blue). THD and THE are in lower L-shell than THA. *Z*-direction is along the magnetic field. Dynamic spectra of simultaneously observed EMIC rising tones are shown for each spacecraft. Though we have scattered source regions, the triangular region in white is the possible source region. Separation of THD to THE spacecraft are one EMIC wavelength (~2,023 km) at ~14:23 UT, suggesting the evolution of the subpacket within one wavelength.

Cluster observations near-equatorial plasmapause, Grison et al. (2013) reported that the triggering process is a repetitive structure, which is a localized phenomenon in space and time. Multispacecraft observations showed these rising tone emissions could be generated slightly off the equator (Grison et al., 2018) and get damped after several reflections. Higher frequencies get reflected from higher MLAT (Grison et al., 2016). Nakamura et al. (2014, 2015) have investigated the rising and falling tones of these waves by THEMIS observations. They have also discussed the nonlinear mechanism to understand the nature of the subpackets. Though they have tried to explain the nonlinear optimum amplitude and the interaction time for the subpackets, they did not indicate the source regions. Spatio-temporal extension of the EMIC rising tone subpackets remained unexplored.

We present a unique study of simultaneous observation of rising tone emissions of EMIC waves on September 09, 2010 from 14:20 to 14:30 UT by THEMIS A (THA), THEMIS D (THD), and THEMIS E (THE). The nonlinear evolution of subpackets in spatial and temporal domains is demonstrated. Also, the existence of the scattered source regions of EMIC waves is explored by using the Poynting vector analysis. The overview of the event is discussed in Section 2. Detailed analysis of the subpackets is reported in Section 3. In Section 4, we support our observations with nonlinear wave growth theory and summarize the results in Section 5.

2. Location of the Spacecraft and Overview of the Event

Figure 1 shows the locations of the spacecraft THA, THD, and THE on 09 September 2010 from 14:20 to 14:30 UT in the outer magnetosphere (L ~ 8 R_E; 1 R_E ~ 6,400 km). THA was in the higher L-shell (~8.2–8.95 R_E) than the other two spacecraft (~7.8–8.6 R_E). The RS93 magnetopause model (Roelof & Sibeck, 1993) is used to estimate the position of the magnetopause. THA was at a position ~2.35 R_E away from the magnetopause whereas THD and THE were at ~2.7 R_E. THA was located at ~1.4°–2.8° MLAT whereas THD and THE were at ~4.1° to 5.2° MLAT. The event is at the pre-dusk sector as the spacecraft observations were taken during ~12.8–13.25 h MLT. The formation of the three THEMIS probes is THA to THE to THD along the magnetic field line from south to north.

In Figure 2, we present the schematic during the event at respective locations. In the inset, the distances (in R_E) of THA (black), THD (magenta), and THE (blue) from the Earth are plotted. EMIC wave subpackets are simultaneously observed by all the three: THA, THD, and THE. THA is 3,552 km and 3,310 km away from THD and THE, respectively, whereas THE and THD are ~2,023 km apart. THE and THD are at almost identical L-shell and observe almost the same dynamic spectra. This configuration of the spacecraft provides an excellent platform for multipoint analysis of the EMIC wave event to locate the source regions and establish a spatio-temporal extension of the EMIC subpackets.

We examine the solar wind conditions on 09 September 2010 to understand any variability in the magnetosphere. The solar wind parameters are shown in Figure 3. At the time of the event, the interplanetary magnetic field (IMF) components B_x, B_y, and B_z (Figures 3a–3c, respectively) appear to be stable; however, we can observe a rotation in the B_z

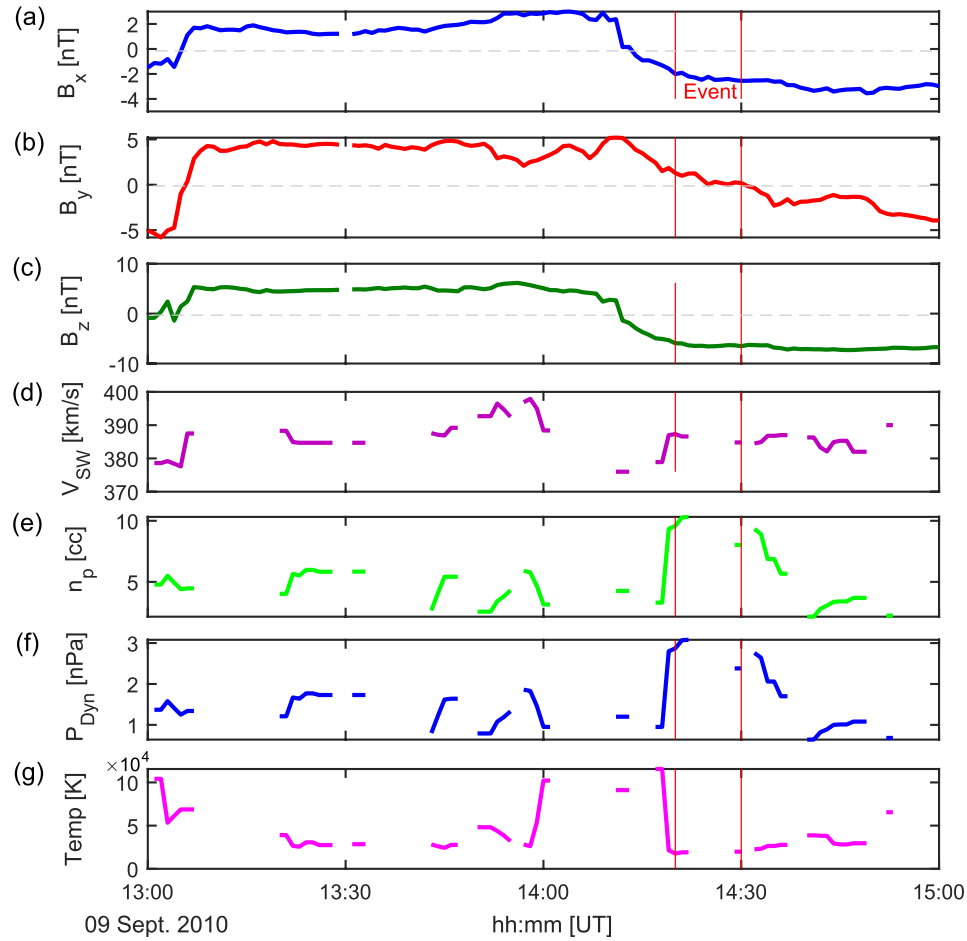

Figure 3. Solar wind parameters from OMNIWEB: The figure demonstrate solar wind parameters observed from OMNI dataset; (a), (b), and (c) represent B_x, B_y, and B_z interplanetary magnetic field (IMF in nT) in GSE coordinates, respectively (d) The solar wind flow speed V_{SW} (km/s) (e) Proton density n_p (cm^{-3}), (f) dynamic pressure P_{Dyn} (nPa) and (g) Proton temperature (Kelvin). Two red vertical lines are start and end timings of the event, i.e., 14:20 UT to 14:30 UT.

component suggesting a dayside magnetic reconnection at the magnetopause just ahead of the event. This could be indicative of the dayside injection of the particles. There are data gaps in other solar wind parameters; still, we can infer that the flow speed (V_{SW}) was ~385 km/s (Figure 3d). The solar wind proton density (n_p) increased significantly from ~2 cm^{-3} to 10 cm^{-3} (Figure 3e), leading to an increase in solar wind dynamic pressure (P_{Dyn}) from 1 to 3 nPa (Figure 3f) just ahead of the event, which is suggestive of the magnetospheric compression. As shown in Figure 3g, the proton temperature has decreased from 12,000 to 2,000 K. These magnetosphere compression conditions lead to the generation of temperature anisotropy, which is known to be a favorable condition for the generation of EMIC waves (Blum et al., 2021; Kakad et al., 2019). Recently, Grison et al. (2021) have shown that the higher occurrence of EMIC waves in the magnetosphere depends upon the distance from the magnetopause.

3. THEMIS Observations

We have used THEMIS fluxgate magnetometer (FGM) (Auster et al., 2008) and electric field instrument (EFI) (Bonnell et al., 2009) data to analyze EMIC wave spectra and their properties. FGM provides both low (4 Hz) and high (128 Hz) resolution data for the magnetic field (B-field) with an accuracy of 0.01 nT. The background trend of the magnetic field measured by FGM is then subtracted from the raw field to obtain the waves. EFI instrument in THEMIS provides two perpendicular components of electric field (E-field), and the parallel component, E_z is obtained by assuming $\mathbf{E}\cdot\mathbf{B} = 0$ and thus $E_z = -((B_x/B_z)E_x + (B_y/B_z)E_y)$.

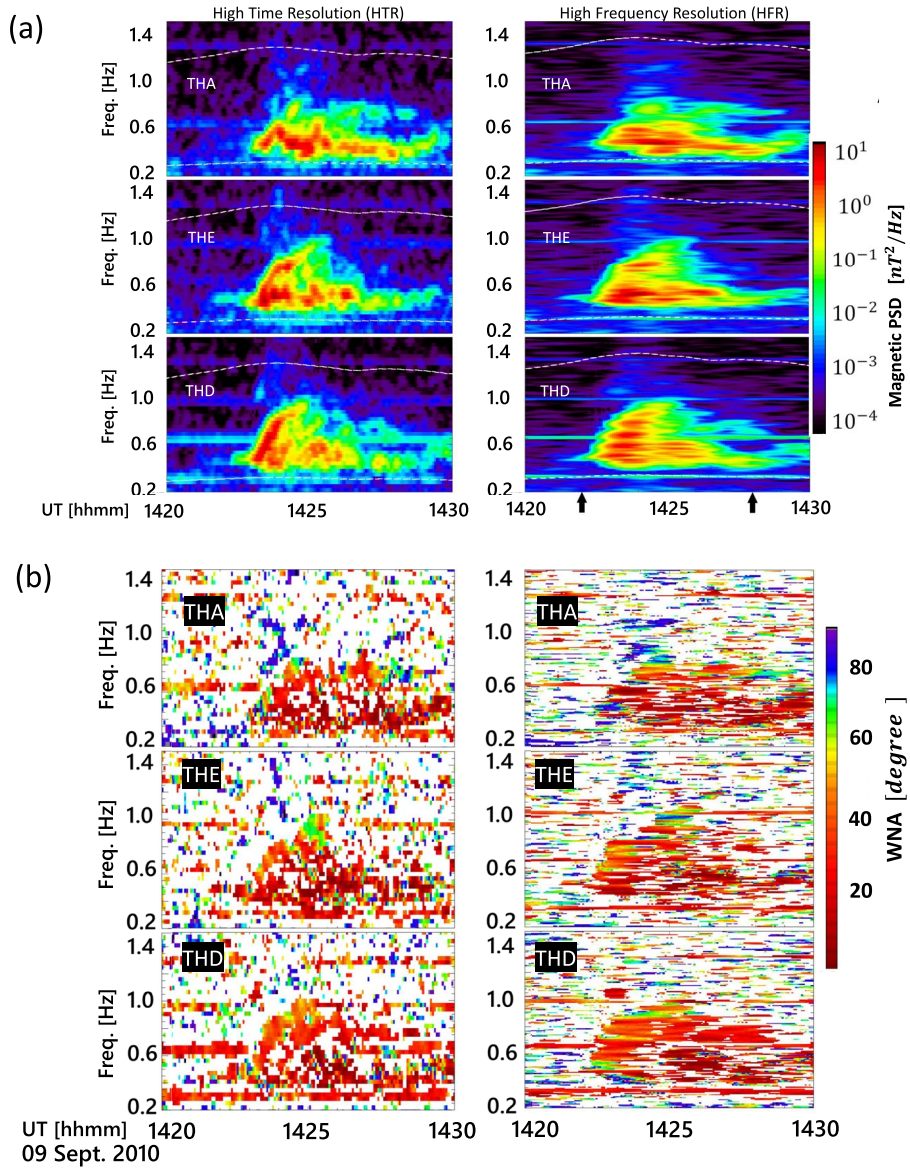

Figure 4. (a)THEMIS A E D Dynamic power spectra of total wave magnetic field (B_w) observed on September 9, 2010. left: High time resolution (HTR) -window size of 32 s (128 samples) and right: High frequency resolution (HFR): window size of 128 s (512 samples) with shifting window by 4 s (16 samples); The exact timings of the rising tones are determined by HTR, where HFR demonstrate duration of the subpackets. The upper (lower) white dashed lines are local proton (helium) gyrofrequencies. The black arrows at the bottom of the HFR spectrum at 14:22 UT and 14:28 UT indicate the period of interest; (b) same as (a) but for Wave normal angle spectra with the color bar shows in degree.

We use FGM data with 4 Hz resolution for B-field whereas the E-field data (full mode data 'eff'; see Bonnell et al., 2009) are downsampled from 8 to 4 Hz. A spectral matrix is formed from the band-pass filtered three-component magnetic field and three-component electric field data. We use the SPEDAS programming (http://spedas.org/blog) for analyzing the wave polarization, ellipticity, and WNA for this event (Means, 1972; Samson & Olson, 1980).

To compute the power spectral density (PSD) of B-wave field by FFT, we use high time resolution (hereafter HTR) with window size of 32 s (128 samples) and high frequency resolution (hereafter HFR) with a window size of 128 s (512 samples). In both cases, we shift the FFT window by 4 s. We can identify different rising tone emissions in different timings in the HTR spectrum and identify subpackets in one emission for different frequencies in the HFR spectrum. Figure 4a represents both HTR (left panels) and HFR (right

Table 1
Spacecraft Separation in Kilometers in GSM Coordinate From Start Time (st) 14:20 UT to End Time (et) 14:30 UT

Start time (st) and end time(et)	Spacecraft separations in km		
	A to D	A to E	E to D
Z_{st} ($\parallel B_0$)	2,907	2,642	266
Z_{et}	2,880	2,591	289
X_{st} ($\perp B_0$)	−1,945	−1,473	−472
X_{et}	−1,900	−1,404	−496
Y_{st} ($\perp B_0$)	599	−1,344	1,941
Y_{et}	637	−1,316	1,953
XY_{st} ($Plane \perp B_0$)	2,035	1,994	1,997
XY_{et}	2,004	1,924	2,014

panels) dynamic spectra for the magnetic field and the corresponding WNA in Figure 4b. The legend for magnetic spectra shows the PSD in nT^2/Hz. These subpackets are identified in HFR panels as island like structures. The rising tone EMIC waves have smaller fine structures rather than monotonically increasing frequency and amplitude. They are repetitive structures of short wavepackets forming a rising tone (Nakamura et al., 2015; Shoji & Omura, 2013). The upper and lower white dashed lines in Figure 4a represent the local proton and helium gyrofrequencies, respectively. In both Figures 4a and 4b, panels are arranged from top to bottom for THA, THE, and THD, respectively, that is, tracing from the southernmost (THA) to the northernmost (THD). The same sequence is followed in the subsequent Figures 5–7 and 10. We have identified each subpacket at different frequencies by increasing the frequency resolution, whereas the timing of the emissions had to be determined by looking at the HTR spectrum. The dynamic spectra of HTR in all the three spacecraft observations show the main rising tone at ~14:23 UT and another one at ~14:24 UT and a few more subsequently. This distinction is very clear for THD, though it is not so demarcated for the other two spacecraft. Being closer along the magnetic field line (refer to Table 1), THD and THE observe almost the same dynamic spectrum. The frequency extension for THD and THE is from ~0.4–1.0 Hz, whereas for THA, the high-frequency emission (0.7–1 Hz) has a lower maximum intensity than the low-frequency emissions. HFR spectrum for THD distinctly show at least six subpackets stacking from low to high frequency at ~14:23 UT, and among these subpackets, the low-frequency subpackets are present for the other two spacecraft, THA and THE. The black arrows at the bottom of the HFR spectrum at 14:22 UT and 14:28 UT indicate the period of interest. Figure 4b shows WNA spectra for both HTR and HFR, where most of the frequencies have WNA $\leq 30^\circ$.

Figure 5 presents the wave magnetic field components in field aligned coordinates (FACs) for THA, THE, and THD. In FACs, *X*-axis is along the Sun-Earth line, *Z*-axis is parallel to the Earth's magnetic field and *Y*-axis completes the orthogonality. We have used the FGM level 1 (L1) raw magnetic field data and processed it with a band-pass filter from 0.35 to 1.2 Hz. It is observed that the waves are highly coherent (~90% coherency), left hand polarized, and WNAs are $\leq 30^\circ$. These observations are consistent with the typical EMIC wave properties. We identify the wave packets (pointed by the black arrows), where FAC-X, FAC-Y, and FAC-Z components of the wave magnetic fields are shown in blue, green, and red colors, respectively.

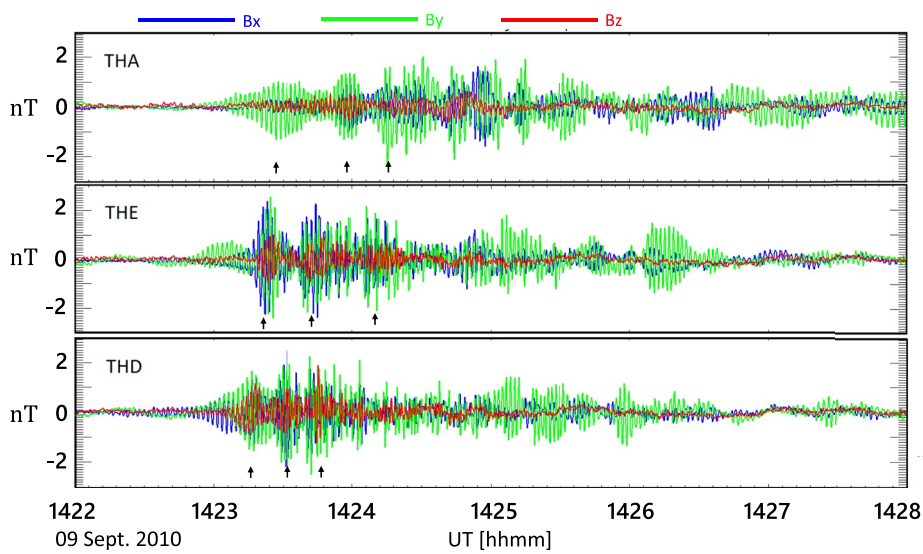

Figure 5. The figure represents the rotated wave magnetic field components for three spacecraft. We have used fluxgate magnetometer level 1 (L1) raw magnetic field and processed the data with band pass filter from 0.35 to 1.2 Hz. Then the magnetic field is transformed to field aligned coordinate. Black arrows indicate subpackets or wavepackets.

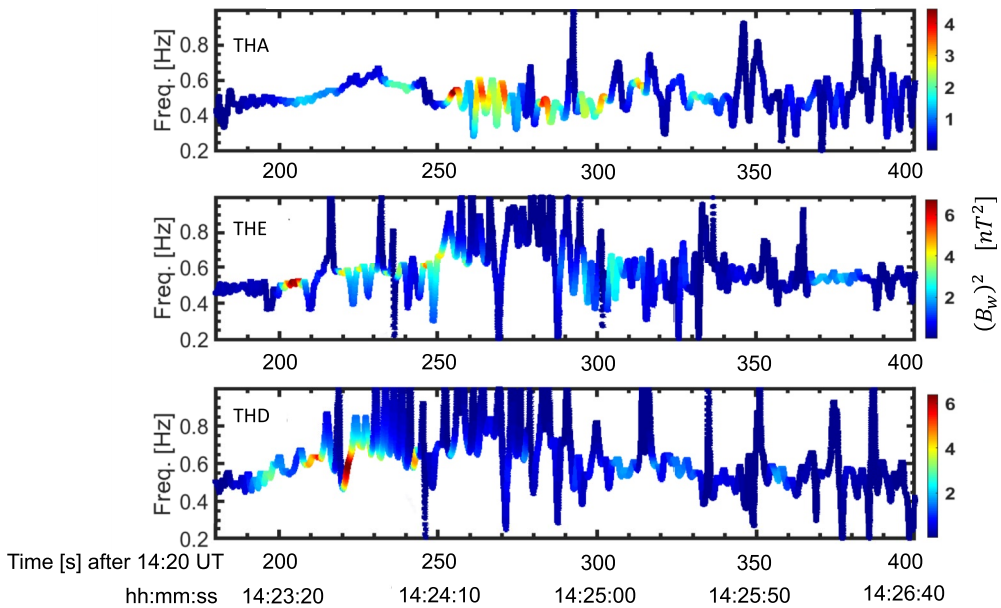

Figure 6. Instantaneous frequency and instantaneous amplitude were obtained from Hilbert Huang transformation for the observed Electromagnetic Ion Cyclotron event by THA, THE and THD on September 9, 2010. Frequency rising is shown with the frequency versus time plot where the color bar shows the square of the instantaneous amplitude (B_w^2).

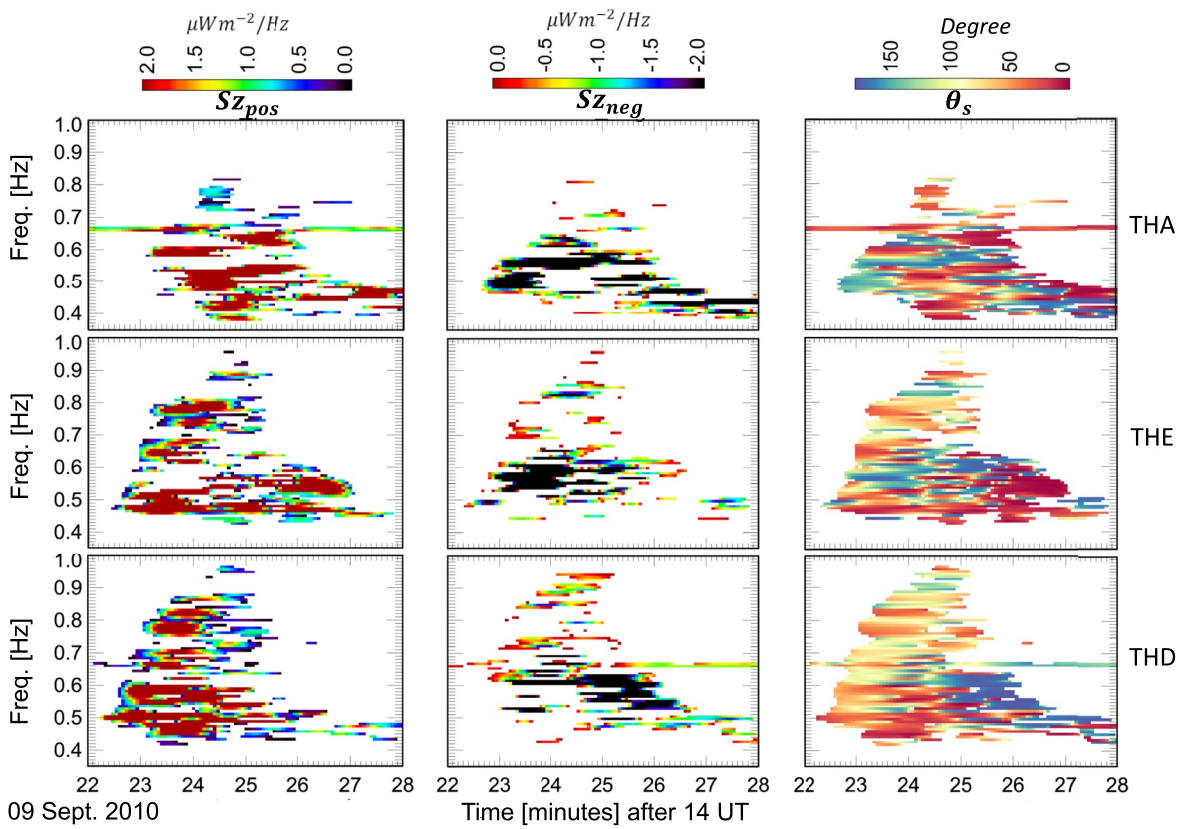

Figure 7. Parallel Poynting flux (S_Z) for THA,THE, and THD (top to bottom): left (middle) panel shows S_Z positive (negative) and the right most panel shows the Poynting angle θ_S(angle between the Poynting vector and the background magnetic field).

The wave components are shown from 14:22 UT to 14:28 UT. The perpendicular wave components are dominant over the parallel component, which is typical for EMIC waves with small WNA. The radial and parallel components are almost comparable for THE and THD. It suggests that THE and THD have larger parallel magnetic fields and higher WNAs. THE and THD observed more obliquely propagating waves than THA as they have slightly larger parallel magnetic field components. The propagation properties of these wave packets are discussed later in the paper.

The instantaneous frequency and amplitude are analyzed by using Hilbert Huang Transformation (HHT) for the three spacecraft. The HHT is an application to analyze nonlinear and non-stationary waveforms in various scientific domains (Huang, 2014; Huang & Wu, 2008; Huang et al., 1998). Primarily, the waveforms are decomposed into several intrinsic mode functions which are further analyzed by the Hilbert spectral analysis for instantaneous frequencies. Instantaneous frequencies are obtained by taking the time derivative of the phase of the analytic signals whereas the instantaneous amplitude are the amplitudes of the analytic function. The instantaneous frequency analysis of the rising tones is commonly used (Kurita et al., 2012; Omura et al., 2010; Santolík et al., 2003, 2004, 2014). Recently, Shoji et al. (2018) applied HHT for one of the EMIC wave events observed by the ARASE satellite and showed the rising tone sweep rate accurately matches with the nonlinear wave growth theory (Omura et al., 2010). We plot the instantaneous frequency as a function of time with the color bar showing the square of the instantaneous wave amplitude in Figure 6. The horizontal axis spans the time interval 180–400 s after starting of the event that is, 14:20 UT. It is observed that the rising of the frequency starts above 0.4 Hz for all the spacecraft in the same time window. THD is showing the highest slope as compared to THA and THE. Further, Figure 6 shows the primary amplitudes are nearly the same, and similar linear growth in all the spacecraft at low frequency. Thereafter, the nonlinear growth process started, and frequency rose rapidly. The present analysis is consistent with the dynamic spectrum from the FFT analysis. The maximum value of instantaneous wave amplitude was observed for THE at 200 s and for THD at 210 s after 14:20 UT. The maximum amplitude for THA, which is observed for 250–300 s after 14:20 UT, indicates the wave packets which are not associated with the main rising tone at 14:23 UT. The second rising tone emission is observed between 250 and 300 s after 14:20 UT. To support these results, we demonstrate the nonlinear transition time in the next section.

Figure 7 depicts Poynting vector analysis for the observed EMIC waves. The three components of the Poynting vector (S_x, S_y, and S_z) and the total Poynting vector (S_{tot}) are obtained by using the method followed by Loto'Aniu et al. (2005) and Santolík et al. (2010). In Figure 7, the parallel and anti-parallel components of the Poynting vector, that is, Sz_{pos}, the component parallel to the background magnetic field (northward, we name it as a forward wave) and Sz_{neg}, the component anti-parallel to the background magnetic field (southward, we name it as a backward wave) are plotted in left and middle panels, respectively. Also, for THA, THE, and THD, θ_S (the angle between Poynting vector and magnetic field) is plotted in the rightmost panels. It is observed from the left and middle panels that both forward and backward EMIC waves are present. It suggests the bi-directional propagation of EMIC subpackets near the magnetic equator. Sz_{pos} is plotted from a scale 0–2.0 $\mu W/m^2/Hz$ and Sz_{neg} is plotted from -2.0 0 $\mu W/m^2/Hz$.

Looking at the panels for THA, it is noted from Sz_{pos} that the subpackets in red at 0.4 Hz, 0.5 Hz, 0.6 Hz, and 0.65 Hz are moving northward, having $\theta_S \sim 20°$ or below showing almost parallel propagation with lower WNA. Looking at the timing and the frequency extent of the main rising tone, the subpacket at 0.65 Hz may be related to the second rising tone. On the other hand, in Sz_{neg} panel, the southward propagating subpackets in black are highly anti-parallel to the background field having smaller WNA and θ_S. The horizontal line at 0.66 Hz is the second harmonic of the spacecraft spin frequency, which is 0.33 Hz for THEMIS.

For THE, we observe the forward waves at 0.5 Hz having $\theta_S < 20°$ but at 0.7 and 0.8 Hz θ_S is $\sim 90°$, whereas the WNAs are $< 30°$. This can be explained as the superposition of a large number of forward and backward waves present there, where the parallel components almost cancel each other and θ_S becomes oblique. For backward waves in THE, we can clearly observe the anti-parallel θ_S around 0.5–0.6 Hz. We note that frequencies 0.6–0.8 Hz in THE are missing in the middle panel of Figure 6. The HFR spectrum for THE in Figure 4a shows less power between 0.6 and 0.8 Hz during 210–220 s after 14:20 UT. The HHT method used here assumes an analytical function to calculate the instantaneous frequency. This discontinuity of higher value of wave power is interpolated (here spline interpolation is used); as a result, a sudden peak between 210 and 220 s is seen in Figure 6 for THE.

Finally, in THD, which is the northernmost spacecraft in this event, at least six forward subpackets show $\theta_S \simeq 50° - 90°$. In this case, the WNA at different frequencies is $\sim 40° - 60°$ including at 0.5 Hz where WNA $\simeq 90°$. A smaller number of backward waves are present except at 14:25 UT to 14:27 UT, which is not the primarily triggered emission (at 14:23 UT). This suggests THD has more oblique waves propagating northward, and maybe THD is slightly away from the source region.

The striking feature of the Poynting flux analysis is the near absence of backward waves (southward) above 0.6 Hz, though we observe subpackets for Sz_{pos}, that is, forward (northward) propagating waves. Also, 0.6 Hz $= f_{cp}/2$, which further suggests there is an absence of backward (southward) waves above half gyrofrequency. Discussion of this exciting feature is beyond the scope of this paper and will be investigated in future studies.

4. Comparison of the Observations With Nonlinear Wave Growth Theory

A comparison of observations with nonlinear wave growth theory is made for a better understanding of the results. We consider the cold plasma dispersion relation (Stix, 1962) with three cold ion populations (H^+, He^+ and O^+), electrons (e^-), and hot protons. THEMIS does not have an on-board mass spectrometer; therefore, we use the local cutoff frequencies of the L-mode EMIC waves in the generation region. We further assumed that the composition of densities are the same at both generation region and local observation region. This method is discussed in Omura et al. (2010). The composition of the plasma is as follows: $(n_H : n_{He} : n_O) \Rightarrow (0.88 : 0.06 : 0.06)$ and 0.1% hot H^+ of total proton density. The total electron density $n_e = 6$ cm^{-3} is nearly the same for all the spacecraft observations. The average DC magnetic field at the time of the event is ~85 nT and corresponding proton gyrofrequency $(f_{cp}) = 1.3$ Hz. Though the EMIC generation condition suggests the minimum magnetic field gradient or minimum B-pockets at the generation region, we observe the maximum value of the background magnetic field during 14:20 UT to 14:30 UT. This may be due to the magnetospheric compression during the event, which further increases the density.

We calculate the wavelength ($\lambda = 2\pi/k$, k is wave number) of observed EMIC waves by assuming parallel propagation. Figure 8a shows the variation of λ as a function of wave frequency for electron densities (n_e) 4, 6, and 8 cm^{-3} in green, black, and red colors, respectively. This is very important to analyze the relationship between the subpacket extension and spacecraft separation. We show proton band where a gradual decrease of wavelength is observed with increasing frequency. For, $n_e = 8$, 6, and 4 cm^{-3}, we note that the $\lambda = 2{,}000$, 2,500, and 3,000 km, respectively, at ~0.5 Hz and $\lambda = 1{,}200$, 1,350, and 1,650 km, respectively, at 0.6 Hz. Further, for the higher frequencies (>0.6 Hz), the wavelengths of EMIC waves are $\leq$ 1000km.

We tabulate the spacecraft separation in Table 1. The measured separation for THE to THD along Z_{GSM}, i.e., along the magnetic field line ($\| B_0$), varies from 266 to 289 km. This separation is much less than wavelength, λ_{EMIC} of the EMIC waves. X_{GSM} varies from 472 to 496 km, whereas Y_{GSM} varies slightly from 1,941 to 1,953 km. The last row in Table 1 shows the spacecraft separation in XY plane (perpendicular plane to B_0). The separation between THE and THD in the XY plane is greater than that in the parallel direction. The WNA analysis shows that the wave packets for THE and THD are propagating with WNA $\leq 30°$. This suggests the perpendicular component of the wave number (i.e., $k_\perp$) is smaller than the parallel component ($k_\|$), and one could expect similar wave power and coherency between THE and THD.

We have calculated the radial separation δR $(= \sqrt{X^2 + Y^2 + Z^2})$ of the spacecraft for the duration of the event, that is, 14:20–14:30 UT. The radial separation between THD to THE varies from 2015 to 2,070 km, THA to THE varies from 3,310 km to 3,227 km, and THA to THD varies from 3,549 to 3,509 km. Further, the radial separation between THD and THE at the time of triggered rising tone emission, that is, at 14:23 UT is ~2,023 km, whereas between THA and THE is ~3,300 km. Thus, it is an excellent multipoint analysis platform to understand the simultaneous observation of EMIC subpackets over thousands of kilometers. These observations show the evolution of EMIC subpackets within one wavelength as the λ_{EMIC} varies from ~4,000 km–500 km (from low frequency to high frequency).

We theoretically estimate the wave energy by using the cold plasma approximation. Using charge neutrality condition, the group velocity of the EMIC waves from Eq. (22) of Omura and Zhao (2012),

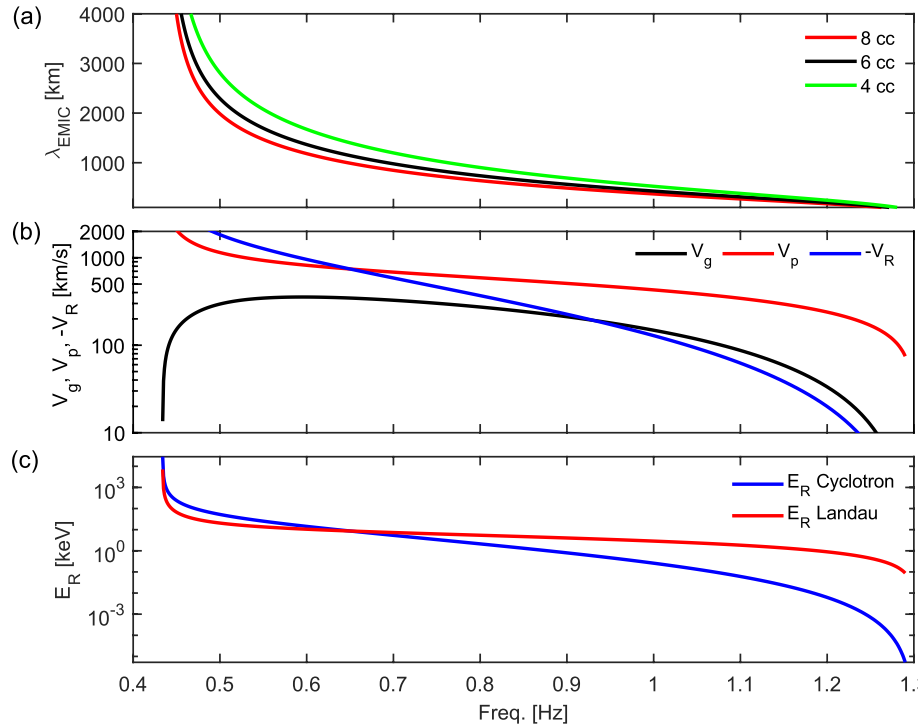

Figure 8. (a) Wavelength (λ_{EMIC}) is plotted versus frequency for proton band (H^+-band) for electron density (n_e) 4, 6, and 8 cm^{-3} (green, black, and red line, respectively); (b) Assuming the cold plasma dispersion (Stix, 1962) and using the observed densities and background magnetic field group velocity (V_g) (black), phase velocity (V_p) (red), and negative resonance velocity ($-V_R$) (blue) are plotted; (c) Cyclotron resonance energy (blue) and Landau resonance energy (red) is plotted w.r.t. frequency for proton band assuming the isotropic proton distribution. Panel (b) and (c) are plotted with $n_e = 6\ cm^{-3}$.

$$V_g = \frac{2c^2k}{\omega}\left[\sum_s \frac{\omega_{ps}^2\,(2\Omega_s - \omega)}{\Omega_s(\Omega_s - \omega)^2}\right]^{-1}. \tag{1}$$

where s = H^+, He^+, and O^+, c is the speed of light, k is the wave number, ω is the angular frequency of the wave, ω_{ps} and Ω_s are the plasma and gyro frequencies of the species 's'.

The wave group velocity, V_g (black solid curve), phase velocity, V_p (red solid curve), negative resonance velocity, $-V_R$ (blue solid curve) are plotted as a function of frequency in Figure 8b. A significant increase in group velocity is observed for H^+-band waves which maximizes at ~0.6 Hz with V_g ~356 km/s. The waves are evolving with phase velocity, V_p ~500 km/s at the highest value of V_g. The gradient in V_g is low at ≥0.6 Hz, which further support the loss of wave energy above 0.6 Hz.

The phase velocity V_p also decreases with the increasing frequency. Assuming the first order cyclotron resonance condition and parallel propagation, we have the resonance velocity,

$$V_R = \frac{\omega - \Omega_{cp}}{k_\parallel}, \tag{2}$$

where Ω_{cp} is the cyclotron frequency of protons. Figure 8b shows the plotting $-V_R$ for the counter-streaming protons. We find $-V_R > V_g$ in the frequency range of the observed EMIC emissions. Figure 8c shows the plotting cyclotron resonance energy (E_R Cyclotron) (blue) and Landau resonance energy (E_R Landau) (red). The minimum resonant energy (E_R) is weakly decreasing function of frequency around 0.6 Hz as can be seen in Figure 8c. We find $V_p \gg V_g$, which indicates that in the frame of reference moving with the group velocity, the phase of the quasi-parallel wave moves rapidly, making it difficult to have effective nonlinear

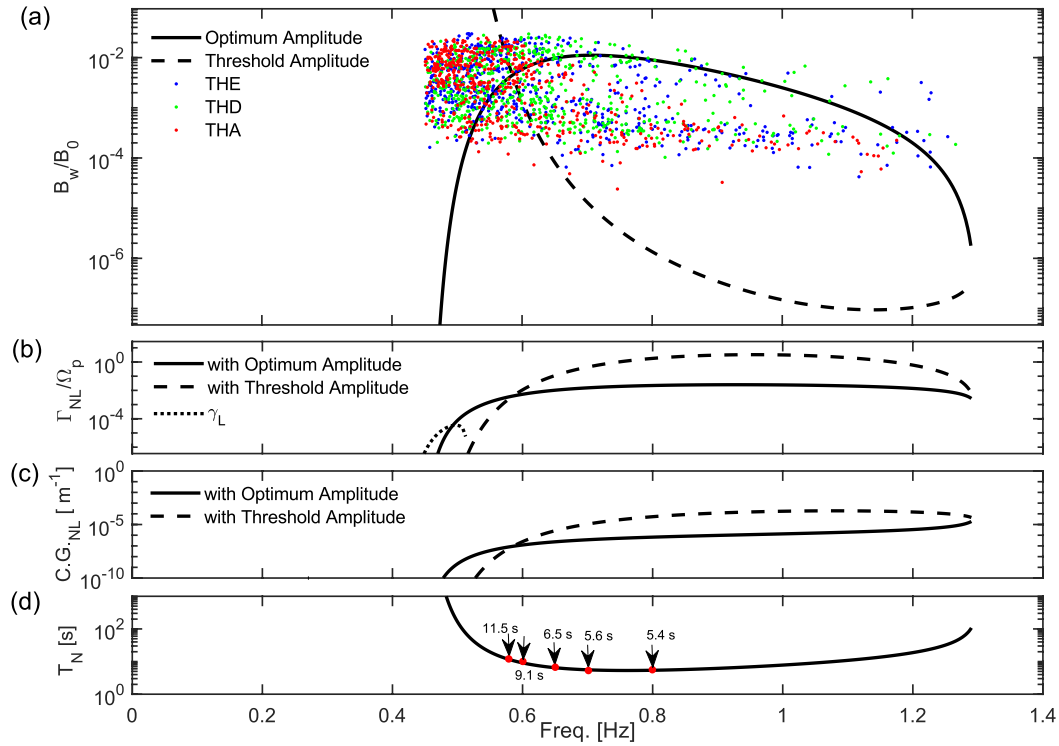

Figure 9. (a) Optimum wave amplitude (solid line) of the Electromagnetic Ion Cyclotron (EMIC) triggered emissions and theoretical threshold amplitude (dashed line) given by Eq. (54) of Omura et al. (2010) as functions of the frequency (shown only for H^+-band). Instantaneous amplitudes as function of instantaneous frequency for THA (red dots), THD (green dots), and THE (blue dots) are over plotted. Observed amplitudes of the EMIC subpackets are well correlated with the theoretical amplitudes. (b) Nonlinear growth rate (Γ_{NL}) using optimum amplitude (solid line) and threshold amplitude (dashed line). γ_L represents linear growth rate (dotted curve), (c) Convective growth rate ($C.G_{NL} = \Gamma_{NL}/V_g$) rate using optimum amplitude (solid line) and threshold amplitude (dashed line), and (d) The nonlinear transition time $T_N = \tau T_{tr}$ as a function of the frequency. T_N is well correlated with the observed subpacket durations. Black arrows with red dot shows T_N values for frequencies 0.58 Hz, 0.6 Hz, 0.65 Hz, 0.7 Hz, and 0.8 Hz. (All the plots in this figure shown for $n_e = 6$ cm^{-3}).

trapping of energetic protons by the wave packet through Landau resonance. We have compared these theoretical energies with the observed proton energies later in this article.

We investigate the optimum and the threshold amplitudes of the observed rising subpackets. We adopt the theory developed by Omura et al. (2010), Shoji and Omura (2013) for this understanding. According to their theory, when a triggered wave (with frequency f_1), which is locally generated because of some temperature anisotropy, exceeds the threshold amplitude, it arranges a gyro-phase around the proton hole in phase space. The counter streaming protons are trapped in this hole, and in the process of this nonlinear interaction between the triggered wave and the particles, a new triggered wave is released with a greater frequency (f_2, where $f_2 > f_1$) and greater amplitude. This new wave can interact again with the incoming protons to make them phase-bunched, and again new triggered wave can generate with high frequency and greater amplitude. This is a chain of self-sustaining nonlinear processes, and the trains of rising subpackets are formed. After exceeding the threshold amplitudes, the subpackets reach an optimum value called the optimum amplitude of the wave growth. We plot the optimum amplitude (solid black curve) and the threshold amplitude (dashed black curve) in Figure 9a.

We use particle velocities $V_\parallel = 420$ km/s and $V_\perp = 540$ km/s observed from the particle data of THEMIS Electrostatic Analyzer (ESA). We have assumed the proton hole is 50% filled (Shoji & Omura, 2013) and the magnetic field is parabolic in nature. Using these parameters, we find the highest growth in H$^+$-band. We normalize the wave amplitude (B_w) with the background magnetic field B_0 ~85 nT. Though THE and THD observe slightly higher ambient magnetic fields ~90 nT (not shown here), the results remain almost the

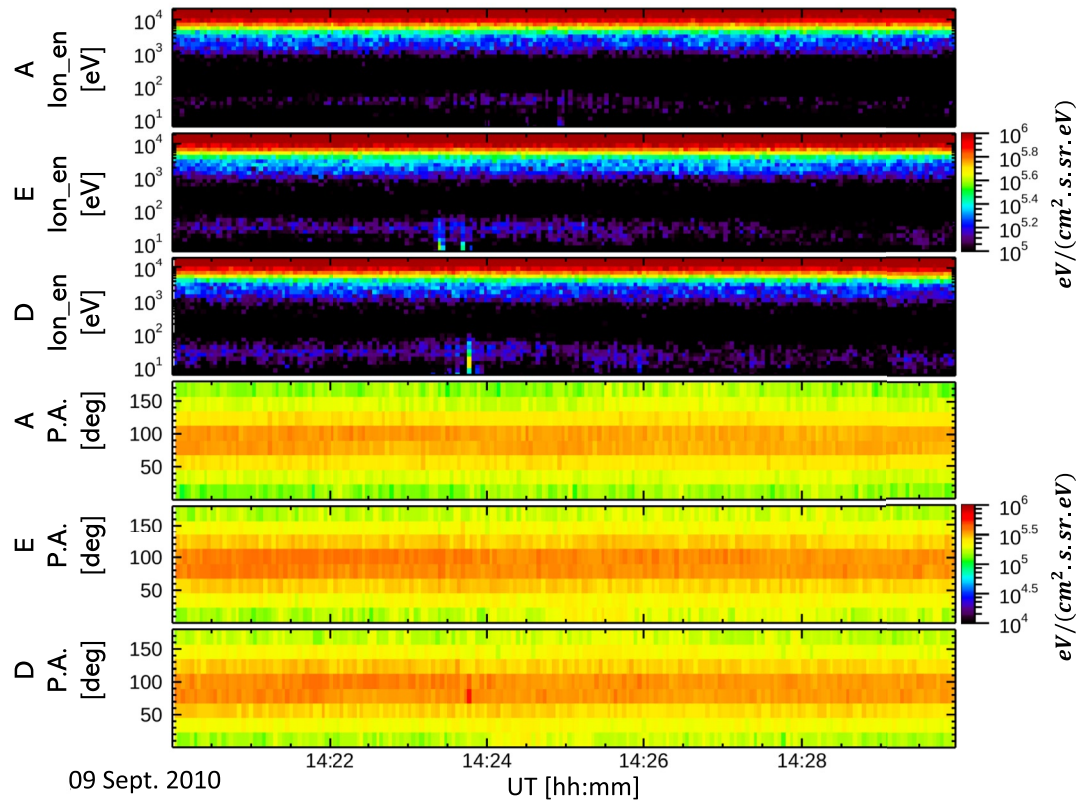

Figure 10. THEMIS A E D ion energy (Ion_{en}) spectra and pitch angle spectra: Top three panels show THA, THE, and THD ion spectra from low to high energy. Enhanced energy flux is seen at ~5–20 keV and this is same for the all the spacecraft. The Pitch angle ($P.A.$) spectra is shown in the bottom three panels, strong flux enhancement around 90° for the all the spacecraft. The upper color bar ($10^5 - 10^6$eV/cm^2.s.sr.eV; for ion energy spectra) and lower color bar ($10^4 - 10^6$eV/cm^2.s.sr.eV; for Pitch angle spectra) shows the energy flux for the protons.

same. The normalized optimum amplitude maximizes to 10^{-2} at ~0.5 Hz. These values also match with the observation in event one of Nakamura et al. (2015).

Instantaneous amplitudes as a function of instantaneous frequency for THA (red dots), THD (green dots), and THE (blue dots) are over plotted in Figure 9a for the proton band EMIC wave. In this plot, each point represents observed instantaneous amplitude (by the HHT method) at a particular instantaneous frequency. We see greater amplitudes for THD and THE than THA at high-frequencies. This suggests there is convective wave growth from THA and THE to THD. For wave frequencies ≥0.58 Hz, observed amplitudes in three spacecraft are mostly above the threshold amplitude obtained by nonlinear wave growth theory. For wave frequencies <0.58 Hz, the observational points are also seen outside of the nonlinear threshold amplitude curve. This could be due to the higher linear growth rate than the nonlinear growth rate for these low frequencies (Figure 9b). For self-sustaining rising tone emissions (Shoji & Omura, 2013), there should be linear growth at the equator where the gradient of the magnetic field is minimum. Thereafter, the nonlinear process starts once the resonant currents generate. Thus, for the lower frequencies, nonlinear wave growth theory has limitations.

Further, we calculate the nonlinear wave growth rate (Γ_{NL}) applying the Eq.(54) of Omura et al. (2010) by considering optimum and threshold amplitudes. In Figure 9b we plot normalized nonlinear growth rate Γ_{NL}/Ω_{cp} that lies between $\sim 10^{-2} - 10^{0}$. In addition, the linear growth rate (γ_L) obtained using the dispersion solver KUPDAP (Sugiyama et al., 2015) with bi-Maxwellian distribution for protons is greater as compared with the nonlinear growth rate in the lower frequency range (Figure 9b, dotted curve). Hence, we conclude the process is well within the nonlinear regime, and the rapid growth of the subpackets is maintained by coherent nonlinear interaction with resonant protons.

Nonlinear Convective wave growth ($C.G_{NL} = \Gamma_{NL}/V_g$) is calculated to show how much these subpackets can grow for different frequencies of EMIC waves. We plot $C.G_{NL}$ as a function of frequency in Figure 9c with both optimum amplitude (solid line) and threshold amplitude (dashed line). Assuming wave amplitudes growing from the threshold to optimum amplitude, we have the nonlinear convective growth rate $\sim (10^{-4} - 10^{-2})$ km^{-1} for waves having frequencies (0.6–0.8) Hz. Thus, the EMIC waves may grow convectively within $(10^2 - 10^4)$ km.

These calculations are compared with the distances of the spacecraft. From Table 1, we see the separation along the magnetic field line between THD to THE is of the order of a few hundred kilometers, whereas for THA to THD or THE is a few thousand kilometers. These separations match very well with the theoretical distances calculated from convective growth rates. For example, the subpacket around 0.8 Hz for THE has less power than THD, and these subpackets are propagating northward (see Figure 4 HFR and Figure 7 Sz_{pos}), suggesting convective wave growth from THE to THD within a few hundred km.

We have calculated nonlinear trapping frequency $\omega_{tr} = \sqrt{kV_{\perp 0}\Omega_w}$ with the theoretical wave number k, observed average perpendicular proton velocity $V_{\perp 0}$ and theoretical wave amplitude Ω_w (here we used calculated optimum amplitudes). Further, we plot in Figure 9c the nonlinear transition time $T_N = \tau T_r$, where $T_r = 2\pi/\omega_{tr}$ is nonlinear trapping period. The transition time is the time taken by the subpackets for the nonlinear interaction in the proton hole. The parameter τ is the ratio of nonlinear transition time to trapping period and is important to investigate the time scale of the nonlinear process. The previous studies (Nakamura et al., 2015; Shoji & Omura, 2013) showed the dependence of optimum and threshold amplitudes on τ and their results matched well with the nonlinear wave growth mechanism for $\tau = 0.5$. We also assume $\tau = 0.5$ in our calculations. The transition time is directly proportional to the observed period of the subpackets or the duration of the subpackets. In Figure 9d, transition times are marked by arrows with red dots corresponding to a set of frequencies. The transition times $T_N = 11.5$ s, 9.1 s, 6.5 s, 5.6 s, and 5.4 s correspond to the frequencies 0.58 Hz, 0.6 Hz, 0.65 Hz, 0.7 Hz, and 0.8 Hz, respectively. The interaction time between the waves with the energetic particles varies from ~(5–12) s. These values also match with the observed durations of the rising tone subpackets.

This interpretation is further supported by the particle (here only proton) measurements from THEMIS-ESA data. We plot the ion energy spectra and the pitch angle spectra in Figure 10 for the observed particle parameters. The top three panels show THA, THE, and THD ion spectra from low to high energies. The color bar shows the energy flux for the protons. The enhanced energy flux at ~5–20 keV is observed for all the spacecraft. These energies are matched very well with the calculated cyclotron resonance energy (E_R Cyclotron) in Figure 8c (blue). This explains that the counter-streaming protons have the required resonance energy in the nonlinear process of self-sustaining rising tones. We also observe the low energy flux enhancement ~30 eV for nearly the whole time window where the maximum can be observed between 14:23 UT to 14:24 UT, which is the event timing. However, the required cyclotron resonance energy is much greater than this low energy enhancement. To resolve this, we calculate the Landau resonance energy (E_R Landau) in Figure 8c (red), but the Landau resonance energy also does not meet with the observations. This can be overcome by adopting the concept of wave-wave interaction. The interaction of the forward and backward traveling wavepackets plays a crucial role in parallel heating which is found in the EMIC instability driven by an ion temperature anisotropy (Omura et al., 1988). We will explore this possibility in future investigations.

The pitch angle spectra are shown in the bottom three panels of Figure 10. We observe strong flux enhancement around 90°, i.e., more energy flux is present perpendicular to the background magnetic field for all the spacecraft throughout the event time interval. These protons are trapped adiabatically in this equatorial zone and favor the nonlinear interaction being phase-bunched in the electromagnetic proton holes in phase space (Omura et al., 2010; Shoji & Omura, 2017). This suggests the three spacecraft are close to the equatorial plane and THA is the closest to the equator. We can say: (a) being the northernmost spacecraft, (b) distinct subpackets at high frequencies, and (c) steeper frequency sweep rate, THD observed clear forward (northward) subpackets because of high convective growth and rapid nonlinear evolution.

5. Discussion and Summary

The technique used in our analysis to identify rising tone emissions and subpacket structures is summarized here. Firstly, it is important to have a visual inspection of both HTR and HFR (refer to Figure 4) spectrum. This way distinction can be made between two separate rising tones and subpackets embedded in a rising tone. The simultaneous observations of rising tone EMIC waves at 14:23 UT by THA, THE, THD are determined from the HTR spectrum whereas subpackets are identified in HFR. They are also identified in the waveforms of the magnetic components for all spacecraft (Figure 5). Further, the instantaneous frequency and amplitudes of the observed rising tone emission and validate it with the nonlinear wave growth theory. Poynting flux analysis provides both forward and backward propagating subpackets. This confirms the spacecraft were inside the source regions of EMIC waves.

As each subpacket is formed in the process of interaction between the triggering waves and the counter streaming protons, multiple source regions are moving upstream toward higher latitudes with higher magnetic field gradients with increasing frequency. Shoji and Omura (2013) found both in theory and simulation, the source region is not static but moves upstream and the movement of the source region is much smaller (~150 km/s.) than the resonance velocity (see their Figures 8 and 9). We provide the first observational evidence of the movement of the source region by analyzing multipoint observations. Each rising tone consists of many subpackets, which are generated by separate sources where nonlinear interaction between the counter streaming protons and triggering wave takes place. In our observations, the subpackets are formed due to the nonlinear wave growth associated with different sources along the field line.

We provide the timeline of the subpackets. The HTR spectrum shows the rising tone starts from 14:23 UT. First THA has observed backward waves from 14:23 to 14:24 UT, and then forward waves from 14:24 to 14:25 UT with higher frequency. For THE, forward waves are observed from 14:23 to 14:23:30 UT and then backward waves from 14:23:30 UT to 14:24 UT. There is another forward wave with a higher frequency present in THE spacecraft from 14:24 to 14:25 UT. In the case of THD, there is another forward wave with a higher frequency present before 14:25 UT and thereafter backward waves which may be associated with second rising tone. Thus, we propose there are scattered source regions where the sign of parallel component of Poynting vector (S_z) changes. In our case, THA is closest to the equator having a shorter frequency extent, then THE has both forward and backward waves, lastly THD being the northernmost spacecraft, we observe all subpackets are forward waves. Thus, it is proposed that to identify the nonlinear evolution of the rising tone subpackets and the extension of the amplification regions, the wavelength of the EMIC waves along with nonlinear wave growth have to be determined besides Poynting flux orientation.

The findings of our analysis are summarized below:

1. THEMIS spacecraft THA, THE, and THD observations of EMIC subpackets and rising tone emissions in the same time window are reported
2. HHT analysis shows the rapid frequency variation with changing wave amplitude
3. The spacecraft separations are of the order of one wavelength (λ_{EMIC}). The subpackets are changing dynamically within one λ_{EMIC} which suggests rapid nonlinear evolution of the EMIC subpackets
4. THE and THD being close to each other (separation in parallel direction <300 km) the subpackets with V_g ~350 km/s are simultaneously observed in both spacecraft
5. Observations are well supported by the nonlinear growth theory, and the subpackets have greater transition time (duration of the nonlinear interaction or duration of the subpackets) (T_N ~12 s) in the low frequency but decrease gradually (T_N ~5 s) for the high-frequency regime
6. Observed wave amplitudes and corresponding instantaneous frequencies are within the theoretical optimum and threshold amplitudes for frequencies >0.58 Hz. The linear growth dominates at lower frequencies and provides the seed of nonlinear growth. Smaller amplitudes for THA and THE at the higher frequencies than THD confirm the convective wave growth at THD
7. Nonlinear convective growth shows the waves can grow within a few 100 km to a few 1,000 km
8. There exist scattered source regions for the rapid nonlinear process. These source regions extend larger than the wavelength of the EMIC waves and one could expect a 3D extent of the source region
9. Observed ion energies and pitch angle spectra of the ion fluxes are consistent with the energy associated with the Landau and cyclotron resonance conditions

In this paper, we assumed parallel propagation in the theoretical calculations though the observation shows oblique wave propagation in some cases. This study can be improved by considering the oblique propagation of EMIC waves.

Data Availability Statement

We have used THEMIS FGM and ESA data available at "https://cdaweb.gsfc.nasa.gov/pub/data/themis/the/" and OMNI database at "https://cdaweb.gsfc.nasa.gov/pub/data/omni/".

Acknowledgments
Biswajit Ojha thanks the Indian Institute of Geomagnetism (IIG), Navi Mumbai, India, for the support to visit RISH Kyoto University, Japan. The research conducted at Research Institute of Sustainable Humanosphere (RISH), Kyoto University, Japan is supported by JSPS KAKENHI Grant 17H06140. Biswajit Ojha acknowledges SSCWeb (https://sscweb.gsfc.nasa.gov/) for using the data to locate THEMIS probes. We acknowledge NASA contract NAS5-02099 and V. Angelopoulos for use of data from the THEMIS Mission. Specifically, K. H. Glassmeier, H. U. Auster, and W. Baumjohann for the use of FGM data, J. W. Bonnell and F. S. Mozer for use of EFI data and C. W. Carlson and J. P. McFadden for use of ESA data. Special thanks to the SPEDAS (http://spedas.org/blog/) for useful routines. Gurbax S. Lakhina thanks Indian National Science Academy, New Delhi for the support under INSA -Honorary Scientist Scheme. Satyavir Singh and Biswajit Ojha would like to thank Dr. Justin Lee for help in determining the proper data set to be used to calculate the Poynting flux. Biswajit Ojha would like to thank Dr. B. Remya of IIG for fruitful discussions.

References

Allen, R. C., Zhang, J. C., Kistler, L. M., Spence, H. E., Lin, R. L., Dunlop, M. W., & André, M. (2013). Multiple bidirectional emic waves observed by cluster at middle magnetic latitudes in the dayside magnetosphere. *Journal of Geophysical Research: Space Physics*, *118*(10), 6266–6278. https://doi.org/10.1002/jgra.50600

Allen, R. C., Zhang, J.-C., Kistler, L. M., Spence, H. E., Lin, R.-L., Klecker, B., et al. (2015). A statistical study of EMIC waves observed by cluster: 1. Wave properties. *Journal of Geophysical Research: Space Physics*, *120*(7), 5574–5592. https://doi.org/10.1002/2015ja021333

Auster, H. U., Glassmeier, K. H., Magnes, W., Aydogar, O., Baumjohann, W., Constantinescu, D., et al. (2008). The Themis fluxgate magnetometer. *Space Science Reviews*, *141*(1), 235–264. https://doi.org/10.1007/s11214-008-9365-9

Blum, L. W., Bonnell, J., Agapitov, O., Paulson, K., & Kletzing, C. (2017). Emic wave scale size in the inner magnetosphere: Observations from the dual van Allen probes. *Geophysical Research Letters*, *44*(3), 1227–1233. https://doi.org/10.1002/2016gl072316

Blum, L. W., Koval, A., Richardson, I. G., Wilson, L., Malaspina, D., Greeley, A., & Jaynes, A. N. (2021). Prompt response of the dayside magnetosphere to discrete structures within the sheath region of a coronal mass ejection. *Geophysical Research Letters*, e2021GL092700. https://doi.org/10.1029/2021gl092700

Bonnell, J., Mozer, F., Delory, G., Hull, A., Ergun, R., Cully, C., et al. (2009). *The electric field instrument (EFI) for Themis* (pp. 303–341). The THEMIS mission. https://doi.org/10.1007/978-0-387-89820-9_14

Clilverd, M. A., Duthie, R., Hardman, R., Hendry, A. T., Rodger, C. J., Raita, T., et al. (2015). Electron precipitation from EMIC waves: A case study from 31 May 2013. *Journal of Geophysical Research: Space Physics*, *120*(5), 3618–3631. https://doi.org/10.1002/2015JA021090

Cornwall, J. M. (1965). Cyclotron instabilities and electromagnetic emission in the ultra low frequency and very low frequency ranges. *Journal of Geophysical Research*, *70*(1), 61–69. https://doi.org/10.1029/JZ070i001p00061

Cornwall, J. M., & Schulz, M. (1971). Electromagnetic ion-cyclotron instabilities in multicomponent magnetospheric plasmas. *Journal of Geophysical Research*, *76*(31), 7791–7796. https://doi.org/10.1029/JA076i031p07791

Engebretson, M. J., Lessard, M., Bortnik, J., Green, J., Horne, R. B., Detrick, D., et al. (2008). Pc1–pc2 waves and energetic particle precipitation during and after magnetic storms: Superposed epoch analysis and case studies. *Journal of Geophysical Research*, *113*(A1). https://doi.org/10.1029/2007JA012362

Engebretson, M. J., Posch, J., Wygant, J., Kletzing, C., Lessard, M., Huang, C.-L., et al. (2015). Van Allen probes, NOAA, GOES, and ground observations of an intense EMIC wave event extending over 12 h in magnetic local time. *Journal of Geophysical Research: Space Physics*, *120*(7), 5465–5488. https://doi.org/10.1002/2015JA021227

Grison, B., Darrouzet, F., Santolík, O., Cornilleau-Wehrlin, N., & Masson, A. (2016). Cluster observations of reflected emic-triggered emission. *Geophysical Research Letters*, *43*(9), 4164–4171. https://doi.org/10.1002/2016gl069096

Grison, B., Hanzelka, M., Breuillard, H., Darrouzet, F., Santolík, O., Cornilleau-Wehrlin, N., & Dandouras, I. (2018). Plasmaspheric plumes and emic rising tone emissions. *Journal of Geophysical Research: Space Physics*, *123*(11), 9443–9452. https://doi.org/10.1029/2018ja025796

Grison, B., Santolik, O., Cornilleau-Wehrlin, N., Masson, A., Engebretson, M., Pickett, J., et al. (2013). EMIC triggered chorus emissions in cluster data. *Journal of Geophysical Research: Space Physics*, *118*(3), 1159–1169. https://doi.org/10.1002/jgra.50178

Grison, B., Santolík, O., Lukacevic, J., & Usanova, M. E. (2021). Occurrence of emic waves in the magnetosphere according to their distance to the magnetopause. *Geophysical Research Letters*, *48*. https://doi.org/10.1029/2020gl090921

Hendry, A., Santolik, O., Miyoshi, Y., Matsuoka, A., Rodger, C., Clilverd, M., & Shinohara, I. (2020). A multi-instrument approach to determining the source-region extent of EEP-driving emic waves. *Geophysical Research Letters*, *47*(7), e2019GL086599. https://doi.org/10.1029/2019gl086599

Horne, R. B., & Thorne, R. M. (1993). On the preferred source location for the convective amplification of ion cyclotron waves. *Journal of Geophysical Research*, *98*(A6), 9233–9247. https://doi.org/10.1029/92ja02972

Huang, N. E. (2014). *Hilbert-Huang transform and its applications* (Vol. *16*). World Scientific.

Huang, N. E., Shen, Z., Long, S. R., Wu, M. C., Shih, H. H., Zheng, Q., et al. (1998). The empirical mode decomposition and the hilbert spectrum for nonlinear and non-stationary time series analysis. *Proceedings of the Royal Society of London. Series A: Mathematical, Physical and Engineering Sciences*, *454*, 903–995. https://doi.org/10.1098/rspa.1998.0193

Huang, N. E., & Wu, Z. (2008). A review on Hilbert-Huang transform: Method and its applications to geophysical studies. *Reviews of Geophysics*, *46*(2). https://doi.org/10.1029/2007rg000228

Jacobs, J., Rostoker, G., & Watanabe, T. (1965). World-wide propagation of impulsive micropulsation activity through the ionosphere. *Nature*, *205*(4966), 61–62. https://doi.org/10.1038/205061a0

Kakad, A., Kakad, B., Omura, Y., Sinha, A. K., Upadhyay, A., & Rawat, R. (2019). Modulation of electromagnetic ion cyclotron waves by pc5 ULF waves and energetic ring current ions. *Journal of Geophysical Research: Space Physics*, *124*(3), 1992–2009. https://doi.org/10.1029/2017JA024930

Kersten, T., Horne, R. B., Glauert, S. A., Meredith, N. P., Fraser, B. J., & Grew, R. S. (2014). Electron losses from the radiation belts caused by EMIC waves. *Journal of Geophysical Research: Space Physics*, *119*(11), 8820–8837. https://doi.org/10.1002/2014JA020366

Kivelson, M. G., & Russell, C. T. (1995). *Introduction to space physics*.

Kurita, S., Katoh, Y., Omura, Y., Angelopoulos, V., Cully, C., Le Contel, O., & Misawa, H. (2012). Themis observation of chorus elements without a gap at half the gyrofrequency. *Journal of Geophysical Research*, *117*(A11). https://doi.org/10.1029/2012ja018076

Lee, J. H., & Angelopoulos, V. (2014). Observations and modeling of emic wave properties in the presence of multiple ion species as function of magnetic local time. *Journal of Geophysical Research: Space Physics*, *119*(11), 8942–8970. https://doi.org/10.1002/2014ja020469
Lee, J. H., Min, K., & Kim, K.-S. (2013). Characteristic dimension of electromagnetic ion cyclotron wave activity in the magnetosphere. *Journal of Geophysical Research: Space Physics*, *118*(4), 1651–1658. https://doi.org/10.1002/jgra.50242
Liu, Y. H., Fraser, B. J., & Menk, F. (2013). Emic waves observed by cluster near the plasmapause. *Journal of Geophysical Research: Space Physics*, *118*(9), 5603–5615. https://doi.org/10.1002/jgra.50486
Loto'Aniu, T., Fraser, B. J., & Waters, C. L. (2005). Propagation of electromagnetic ion cyclotron wave energy in the magnetosphere. *Journal of Geophysical Research*, *110*(A7). https://doi.org/10.1029/2004JA010816
Mann, I., Usanova, M., Murphy, K., Robertson, M., Milling, D., Kale, A., et al. (2014). Spatial localization and ducting of emic waves: Van Allen probes and ground-based observations. *Geophysical Research Letters*, *41*(3), 785–792. https://doi.org/10.1002/2013gl058581
McCollough, J., Elkington, S., & Baker, D. (2012). The role of shabansky orbits in compression-related electromagnetic ion cyclotron wave growth. *Journal of Geophysical Research*, *117*(A1), A01208. https://doi.org/10.1029/2011ja016948
McCollough, J. P., Elkington, S. R., & Baker, D. N. (2009). Modeling EMIC wave growth during the compression event of 29 June 2007. *Geophysical Research Letters*, *36*(18). https://doi.org/10.1029/2009gl039985
McCollough, J. P., Elkington, S. R., Usanova, M. E., Mann, I. R., Baker, D. N., & Kale, Z. C. (2010). Physical mechanisms of compressional emic wave growth. *Journal of Geophysical Research*, *115*(A10), A10214. https://doi.org/10.1029/2010ja015393
Means, J. D. (1972). Use of the three-dimensional covariance matrix in analyzing the polarization properties of plane waves. *Journal of Geophysical Research*, *77*(28), 5551–5559. https://doi.org/10.1029/ja077i028p05551
Nakamura, S., Omura, Y., Machida, S., Shoji, M., Nosé, M., & Angelopoulos, V. (2014). Electromagnetic ion cyclotron rising tone emissions observed by Themis probes outside the plasmapause. *Journal of Geophysical Research: Space Physics*, *119*(3), 1874–1886. https://doi.org/10.1002/2013JA019146
Nakamura, S., Omura, Y., Shoji, M., Nosé, M., Summers, D., & Angelopoulos, V. (2015). Subpacket structures in EMIC rising tone emissions observed by the Themis probes. *Journal of Geophysical Research: Space Physics*, *120*(9), 7318–7330. https://doi.org/10.1002/2014JA020764
Omura, Y., Pickett, J., Grison, B., Santolik, O., Dandouras, I., Engebretson, M., & Masson, A. (2010). Theory and observation of electromagnetic ion cyclotron triggered emissions in the magnetosphere. *Journal of Geophysical Research*, *115*(A7). https://doi.org/10.1029/2010ja015300
Omura, Y., Usui, H., & Matsumoto, H. (1988). Parallel heating associated with interaction of forward and backward electromagnetic cyclotron waves. *Journal of Geomagnetism and Geoelectricity*, *40*(8), 949–961. https://doi.org/10.5636/jgg.40.949
Omura, Y., & Zhao, Q. (2012). Nonlinear pitch angle scattering of relativistic electrons by EMIC waves in the inner magnetosphere. *Journal of Geophysical Research*, *117*(A8). https://doi.org/10.1029/2012JA017943
Pakhotin, I., Walker, S., Shprits, Y., & Balikhin, M. (2013). Dispersion relation of electromagnetic ion cyclotron waves using cluster observations. *Annals of Geophysics*, *31*, 1437–1446. https://doi.org/10.5194/angeo-31-1437-2013
Pickett, J. S., Grison, B., Omura, Y., Engebretson, M. J., Dandouras, I., Masson, A., et al. (2010). Cluster observations of EMIC triggered emissions in association with pc1 waves near earth's plasmapause. *Geophysical Research Letters*, *37*(9). https://doi.org/10.1029/2010GL042648
Roelof, E. C., & Sibeck, D. G. (1993). Magnetopause shape as a bivariate function of interplanetary magnetic field B_z and solar wind dynamic pressure, *Journal of Geophysical Research. 98*, A12, 21421–21450. https://doi.org/10.1029/93JA02362
Sakaguchi, K., Shiokawa, K., Miyoshi, Y., & Connors, M. (2015). Isolated proton auroras and pc1/emic waves at subauroral latitudes. *Auroral Dynamics and Space Weather*, *215*, 59–70. https://doi.org/10.1002/9781118978719.ch5
Samson, J., & Olson, J. (1980). Some comments on the descriptions of the polarization states of waves. *Geophysical Journal International*, *61*(1), 115–129. https://doi.org/10.1111/j.1365-246x.1980.tb04308.x
Santolík, O., Gurnett, D., Pickett, J., Grimald, S., Decreau, P., Parrot, M., et al. (2010). Wave-particle interactions in the equatorial source region of whistler-mode emissions. *Journal of Geophysical Research*, *115*(A8). https://doi.org/10.1029/2009ja015218
Santolík, O., Gurnett, D., Pickett, J., Parrot, M., & Cornilleau-Wehrlin, N. (2003). Spatio-temporal structure of storm-time chorus. *Journal of Geophysical Research*, *108*(A7). https://doi.org/10.1029/2002JA009791
Santolík, O., Gurnett, D., Pickett, J., Parrot, M., & Cornilleau-Wehrlin, N. (2004). A microscopic and nanoscopic view of storm-time chorus on 31 March 2001. *Geophysical Research Letters*, *31*(2). https://doi.org/10.1029/2003gl018757
Santolík, O., Kletzing, C., Kurth, W., Hospodarsky, G., & Bounds, S. (2014). Fine structure of large-amplitude chorus wave packets. *Geophysical Research Letters*, *41*(2), 293–299. https://doi.org/10.1002/2013gl058889
Shoji, M., Miyoshi, Y., Omura, Y., Kistler, L. M., Kasaba, Y., Matsuda, S., et al. (2018). Instantaneous frequency analysis on nonlinear EMIC emissions: Arase observation. *Geophysical Research Letters*, *45*(24), 13199–13205. https://doi.org/10.1029/2018gl079765
Shoji, M., & Omura, Y. (2012). Precipitation of highly energetic protons by helium branch electromagnetic ion cyclotron triggered emissions. *Journal of Geophysical Research*, *117*(A12). https://doi.org/10.1029/2012JA017933
Shoji, M., & Omura, Y. (2013). Triggering process of electromagnetic ion cyclotron rising tone emissions in the inner magnetosphere. *Journal of Geophysical Research: Space Physics*, *118*(9), 5553–5561. https://doi.org/10.1002/jgra.50523
Shoji, M., & Omura, Y. (2017). Nonlinear generation mechanism of EMIC falling tone emissions. *Journal of Geophysical Research: Space Physics*, *122*(10), 9924–9933. https://doi.org/10.1002/2017JA023883
Stix, T. H. (1962). *The theory of plasma waves.*
Sugiyama, H., Singh, S., Omura, Y., Shoji, M., Nunn, D., & Summers, D. (2015). Electromagnetic ion cyclotron waves in the earth's magnetosphere with a kappa-maxwellian particle distribution. *Journal of Geophysical Research: Space Physics*, *120*(10), 8426–8439. https://doi.org/10.1002/2015JA021346
Summers, D., Ni, B., & Meredith, N. P. (2007). Timescales for radiation belt electron acceleration and loss due to resonant wave-particle interactions: 2. evaluation for VLF chorus, elf hiss, and electromagnetic ion cyclotron waves. *Journal of Geophysical Research*, *112*(A4). https://doi.org/10.1029/2006JA011993
Summers, D., & Thorne, R. M. (2003). Relativistic electron pitch-angle scattering by electromagnetic ion cyclotron waves during geomagnetic storms. *Journal of Geophysical Research*, *108*(A4). https://doi.org/10.1029/2002JA009489
Summers, D., Thorne, R. M., & Xiao, F. (1998). Relativistic theory of wave-particle resonant diffusion with application to electron acceleration in the magnetosphere. *Journal of Geophysical Research*, *103*(A9), 20487–20500. https://doi.org/10.1029/98JA01740
Thorne, R. M., & Horne, R. B. (1992). The contribution of ion-cyclotron waves to electron heating and sar-arc excitation near the storm-time plasmapause. *Geophysical Research Letters*, *19*(4), 417–420. https://doi.org/10.1029/92GL00089
Thorne, R. M., & Horne, R. B. (1997). Modulation of electromagnetic ion cyclotron instability due to interaction with ring current O+ during magnetic storms. *Journal of Geophysical Research*, *102*(A7), 14155–14163. https://doi.org/10.1029/96JA04019

Thorne, R. M., & Kennel, C. (1971). Relativistic electron precipitation during magnetic storm main phase. *Journal of Geophysical research*, *76*(19), 4446–4453. https://doi.org/10.1029/JA076i019p04446

Tsurutani, B. T., & Lakhina, G. S. (1997). Some basic concepts of wave-particle interactions in collisionless plasmas. *Reviews of Geophysics*, *35*(4), 491–501. https://doi.org/10.1029/97RG02200

Tsurutani, B. T., & Smith, E. J. (1977). Two types of magnetospheric elf chorus and their substorm dependences. *Journal of Geophysical Research*, *82*(32), 5112–5128. https://doi.org/10.1029/ja082i032p05112

Vines, S. K., Allen, R., Anderson, B., Engebretson, M., Fuselier, S., Russell, C., et al.(2019). EMIC waves in the outer magnetosphere: Observations of an off-equator source region. *Geophysical Research Letters*, *46*(11), 5707–5716. https://doi.org/10.1029/2019gl082152

Vines, S. K., Anderson, B. J., Allen, R. C., Denton, R. E., Engebretson, M. J., Johnson, J. R., et al. (2021). Determining emic wave vector properties through multi-point measurements: The wave curl analysis. *Journal of Geophysical Research: Space Physics*, *126*(4), e2020JA028922. https://doi.org/10.1029/2020ja028922

Zhang, X.-J., Li, W., Thorne, R., Angelopoulos, V., Bortnik, J., Kletzing, C., & Hospodarsky, G. (2016). Statistical distribution of emic wave spectra: Observations from van Allen probes. *Geophysical Research Letters*, *43*(24), 12–348. https://doi.org/10.1002/2016gl071158

Zhu, H., Chen, L., Claudepierre, S. G., & Zheng, L. (2020). Direct evidence of the pitch angle scattering of relativistic electrons induced by emic waves. *Geophysical Research Letters*, *47*(4), e2019GL085637. https://doi.org/10.1029/2019gl085637